WARWICK
THE UNIVERSITY OF WARWICK

Original citation:
Adobes-Vidal, Maria, Maddar, Faduma, Momotenko, Dmitry, Hughes, Leslie P. , Wren, Stephen A. C. , Poloni, Laura N. , Ward, Michael D. and Unwin, Patrick R.. (2016) Face-discriminating dissolution kinetics of furosemide single crystals : in situ three-dimensional multi-microscopy and modeling. Crystal Growth & Design, 16 (8). pp. 4421-4429.

Permanent WRAP URL:
http://wrap.warwick.ac.uk/81618

Copyright and reuse:
The Warwick Research Archive Portal (WRAP) makes this work by researchers of the University of Warwick available open access under the following conditions. Copyright © and all moral rights to the version of the paper presented here belong to the individual author(s) and/or other copyright owners. To the extent reasonable and practicable the material made available in WRAP has been checked for eligibility before being made available.

Copies of full items can be used for personal research or study, educational, or not-for profit purposes without prior permission or charge. Provided that the authors, title and full bibliographic details are credited, a hyperlink and/or URL is given for the original metadata page and the content is not changed in any way.

Publisher's statement:
"This document is the Accepted Manuscript version of a Published Work that appeared in final form in Crystal Growth & Design. copyright © American Chemical Society after peer review and technical editing by the publisher.
To access the final edited and published work
http://pubs.acs.org/page/policy/articlesonrequest/index.html ."

A note on versions:
The version presented here may differ from the published version or, version of record, if you wish to cite this item you are advised to consult the publisher's version. Please see the 'permanent WRAP url' above for details on accessing the published version and note that access may require a subscription.

For more information, please contact the WRAP Team at: wrap@warwick.ac.uk

warwick.ac.uk/lib-publications

Face-discriminating dissolution kinetics of furosemide single crystals: In situ three-dimensional multimicroscopy and modeling

Maria Adobes-Vidal,[†] Faduma M. Maddar,[†] Dmitry Momotenko,[†] Leslie P. Hughes,[‡] Stephen A.C. Wren,[‡] Laura N. Poloni,[#] Michael D. Ward [#] and Patrick R. Unwin[,†]*

†Electrochemistry and Interfaces Group, Department of Chemistry, University of Warwick, Coventry, CV4 7AL, United Kingdom, ‡Pharmaceutical Development, AstraZeneca, Macclesfield, SK10 2NA, United Kingdom, #Molecular Design Institute and Department of Chemistry, New York University, 100 Washington Square East, Silver Center, room 1001, New York, NY 1003, United States

Abstract

A versatile *in situ* multi-microscopy approach to study the dissolution kinetics of single crystals is described, using the loop diuretic drug furosemide as a testbed to demonstrate the utility of the approach. Using optical microscopy and scanning ion-conductance microscopy (SICM) in combination, the dissolution rate of individual crystallographically independent crystal faces can be measured quantitatively while providing a direct visualization of the evolution of crystal morphology in real time in three dimensions. Finite element method (FEM) models using experimental data enables quantitative analysis of dissolution fluxes for individual faces and determination of the limiting process – mass transport or interfacial kinetics – that regulates dissolution. A key feature of the approach is that isolated crystals (typically < 60 μm largest characteristic dimension) in solution during dissolution experience high and well defined diffusion rates. The ability to obtain this quantitative information for individual crystal faces suggests a pathway to understanding crystal dissolution at the molecular level and regulating bioavailability, for example, through manipulation of crystal morphology.

***Professor Patrick R. Unwin**

Department of Chemistry, University of Warwick

Coventry, CV4 7AL, United Kingdom

Tel: (+44) (0)24 7652 3264

Email: p.r.unwin@warwick.ac.uk

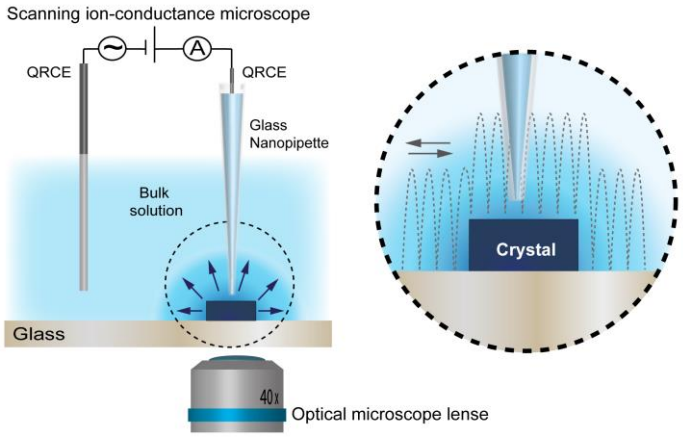

Face-discriminating dissolution kinetics of furosemide single crystals: In situ three-dimensional multimicroscopy and modeling

Maria Adobes-Vidal,[†] *Faduma M. Maddar,*[†] *Dmitry Momotenko,*[†] *Leslie P. Hughes,*[‡] *Stephen A.C. Wren,*[‡] *Laura N. Poloni,*[#] *Michael D. Ward* [#] *and Patrick R. Unwin*[*,†]

†Electrochemistry and Interfaces Group, Department of Chemistry, University of Warwick, Coventry, CV4 7AL, United Kingdom, ‡Pharmaceutical Development, AstraZeneca, Macclesfield, SK10 2NA, United Kingdom, #Molecular Design Institute and Department of Chemistry, New York University, 100 Washington Square East, Silver Center, room 1001, New York, NY 1003, United States

Abstract

A versatile *in situ* multi-microscopy approach to study the dissolution kinetics of single crystals is described, using the loop diuretic drug furosemide as a testbed to demonstrate the utility of the approach. Using optical microscopy and scanning ion-conductance microscopy (SICM) in combination, the dissolution rate of individual crystallographically independent crystal faces can be measured quantitatively while providing a direct visualization of the evolution of crystal morphology in real time in three dimensions. Finite element method (FEM) models using experimental data enable quantitative analysis of dissolution fluxes for individual faces and determination of the limiting process – mass transport or interfacial kinetics – that regulates dissolution. A key feature of the approach is that isolated crystals (typically < 60 μm largest characteristic dimension) in solution during dissolution experience high and well defined diffusion rates. The ability to obtain this quantitative information for individual crystal faces suggests a pathway to understanding crystal dissolution at the molecular level and regulating bioavailability, for example, through manipulation of crystal morphology.

*To whom correspondence should be addressed: Email: p.r.unwin@warwick.ac.uk

Submitted to *Cryst. Growth Des*. April 8, 2016

INTRODUCTION

The majority of active pharmaceutical ingredients (APIs) are small-molecule organic crystals.[1,2] Crystallization is an essential step in their production, wherein the form (i.e. polymorph), crystal morphology, and crystal size impacts processing as well as other important physicochemical properties, including solubility and dissolution rate.[3-5] Dissolution is the first step in drug absorption from the solid form, and it plays a critical role in drug bioavailability.[6,7] Crystals are bounded by faces that are truncations of the three-dimensional lattice along specific crystallographic directions. As such, crystallographically unique faces are expected to exhibit different growth and dissolution behavior. Growth morphologies and kinetics of well-defined crystal faces have been explored using methods such as in situ scanning probe and interferometric microscopies,[8-13] often providing more insightful and accurate measurements of crystal growth than statistical sampling of bulk crystal morphologies.[14] Likewise, measurements of the dissolution kinetics of crystal suspensions that provide average rates of a population of crystals are common,[15-17] but measurements of dissolution of individual crystal faces of single crystals are rare. Mass transport conditions in such systems depend on several parameters that are not easily quantified, including type and speed of the stirrer, vessel and baffle geometry,[18,19] solution density and viscosity, diffusion, crystal morphology, and the quantity and size distribution of the solid particles.[18,20] Mass transport typically is not well defined, to the extent that deducing the kinetic regime can be difficult. Ideally, experimental studies should be configured to allow quantitative local mass transport, from which local undersaturation at the solid/liquid interface and the relationship between surface structure and reactivity can be obtained. Flow cell techniques overcome some of the limitations,[21,22] but typically these are limited to large macroscopic sample areas and particular crystal faces.

These approaches often are not ideal for the dissymmetric character of organic crystal surfaces, which typically are decorated with various crystallographically unique faces, edges, corners and defects that contribute differently to the dissolution process (mechanism and rate). In this respect, near-field microscopies are proving valuable for the study of the dissolution of individual crystals, including atomic force microscopy (AFM),[23-26] optical microscopy,[27,28] and scanning electrochemical microscopy (SECM).[29] Rapid interfacial dissolution kinetics of crystals have been determined by SECM[30] and scanning electrochemical cell microscopy (SECCM).[31] *In situ* interferometry[32] can be useful for determining concentration gradients at crystal/solution interfaces by monitoring changes in the refractive index of the solution, although the minimum detectable concentration difference depends on the minimum fringe shift (ca. 10% of the total concentration change in solution)[33] and interferometric data tend to

represent the average across the studied area. As such, they usually are not suitable for high resolution measurements of heterogeneous reactivity or concentration gradients.

New approaches for assessing dissolution kinetics are essential for the optimization of drug formulations, particular methodologies that permit facile and quantitative characterization of dissolution at a microscopic level that will fill knowledge gaps at the molecular level. Herein we describe a comprehensive approach to real-time characterization of the dissolution of individual faces of single crystals using optical microscopy, scanning ion-conductance microscopy (SICM) and finite element method modeling. SICM is a powerful non-contact method that makes use of a nanopipette for high resolution topographical imaging,[34-36] with the potential to map the dissolution behavior of individual topographical features on crystal surfaces. Collectively, these enable determination of concentration gradients, interfacial concentrations, and separation of kinetic and mass transport limiting regimes. This approach is demonstrated here for the API furosemide (Scheme 1), a loop diuretic drug marketed under the brand name Lasix.[37] Furosemide is a weak acid, classified as a BCS Class IV drug because of its low permeability and poor solubility.[38] Consequently, the bioavailability of furosemide from oral dosage is low (60%) and the rate and extent of absorption varies between and within individuals.[39] It is reasonable to suggest that understanding the dissolution kinetics of furosemide crystals at the microscopic level could lead to strategies for improving its bioavailability and its optimum solid-state form.[3,40-43]

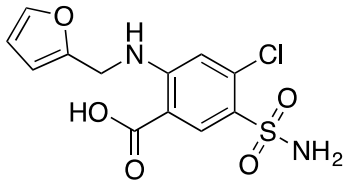

Furosemide

Scheme 1. The molecular structure of furosemide

EXPERIMENTAL

Samples and solutions. Furosemide was purchased from Sigma-Aldrich (>98%, St. Louis, MO) and used as obtained without further purification. Crystals of furosemide were prepared by mixing 0.5 mL of a 10 mM solution of furosemide in ethanol (Sigma-Aldrich, >99.5%) with 3.5 mL deionized (DI) water produced by Purite Select HP with resistivity 18.2 MΩ cm (25 °C) to create a supersaturated solution. The mixture was added by pipette to a 47 mm diameter circular glass microscope slide (Thermo Scientific, Inc., Waltham, MA) previously mounted into a 47 mm diameter Petri dish (Willco Wells,

Netherlands) with a Plexiglas rim, covered, and allowed to stand at room temperature for 15 minutes. The supernatant solution was then removed to reveal small raft-shaped crystals of furosemide, typically < 60 μm long, attached to the glass slide, which was then rinsed with water and dried with a nitrogen stream. All dissolution studies were performed at 25 °C and pH 6.5 in 50 mM KCl (Sigma-Aldrich, AR grade) in ultrapure water. Solution pH was measured with a pH meter (Metler Toledo, Switzerland)).

X-ray characterization. Single crystal X-ray diffraction analysis of furosemide was performed using a suitably large crystal of furosemide (>100 μm) that was mounted on a Mitegen loop with silicon oil and placed on an Oxford Diffraction Xcalibur Gemini diffractometer equipped with a Ruby CCD area detector. The crystal temperature was maintained at 150(2) K during data collection. The crystal structure was solved using Olex2[44] with the ShelXS-2013[45] structure solution program using Direct Methods and refined with the XL refinement package using Least Squares minimization. Powder X-ray diffraction measurements were performed using a Panalytical X'Pert Pro MRD equipped with a hybrid monochromator for CuKα_1 radiation (λ = 1.541 Å). The glass slide on which the furosemide crystals were grown was mounted on the sample holder. A Pixcel detector was used in scanning mode over the range 5° < 2θ < 30°, stepping 0.025° over a period of 45 minutes.

Morphology prediction. To identify the exposed crystal faces, the furosemide crystal morphology was calculated based on the growth morphology method using the Morphology module in Materials Studio (Materials Studio 8.0.100.21, Accelrys, San Diego, CA). The growth morphology method takes into account the energetics of the system and requires the selection of an appropriate forcefield. The geometry of the furosemide unit cell obtained from single crystal CCD X-ray diffraction experiments was optimized using the COMPASS, consistent-valence forcefield (cvff), and Dreiding forcefields and the optimized unit cell with lowest lattice energy and lattice parameters best matching the experimental unit cell was selected for morphology predictions. Geometry optimizations were conducted using the Forcite molecular mechanics tool. The Quasi-Newtown algorithm was used with a convergence tolerance of 2.0×10^{-5} kcal/mol for the energy, 0.001 kcal/mol/Å for the force, and 1.0×10^{-5} Å for the displacement. The Ewald summation method was chosen for the evaluation of van der Waals and electrostatic terms to an accuracy of 0.0001 kcal/mol with a buffer width of 0.5 Å. Forcefield-assigned partial charges were used with the COMPASS and cvff forcefields and the QEq method was used to calculate and assign partial charges with the Dreiding forcefield. The furosemide unit cell optimized with COMPASS was used for the morphology predictions, conducted with a minimum interplanar distance d_{hkl} of 1.300 Å and a maximum Miller Index value (*hkl)* of (333). The maximum number of faces was limited to 200.

Scanning ion-conductance microscopy (SICM). Dissolution investigations were performed by combining optical microscopy and SICM by mounting an SICM system on an inverted optical microscope (Axiovert 40 CFL, Zeiss, Germany). The optical microscope was equipped with an LED light source to reduce sample heating and a video camera (B700, PixeLINK) to assist the selection and monitoring of the crystal. SICM probes (*ca.* 100 nm diameter) were fabricated from borosilicate glass capillaries (1.2 mm o.d., 0.69 mm i.d., Harvard Apparatus, Holliston, MA) using a laser puller (P-2000, Sutter Instruments, Novato, CA) and optimized pulling parameters (Line 1: Heat 350, Fil 3, Vel 30, Del 220, Line 2: Heat 350, Fil 3, Vel 40, Del 180, Pul 120). The nanopipettes were filled with the same electrolyte solution (50 mM KCl) as the aforementioned solution used for dissolution studies. An Ag/AgCl quasi-reference counter electrode (QRCE) was inserted into the nanopipette and another was submerged in the petri dish bulk solution. The nanopipettes were mounted on a 38 μm – travel range single axis (*Z*) piezoelectric positioner (P-753-3CD, PhysikInstrumente, Germany) to control the height of the probe and oriented normal to the surface of interest, as previously described.[46] The petri dish containing the furosemide crystals was mounted on a two-axis (*XY*) piezoelectric positioner system (Nano-BioS300, Mad City Labs Inc., Madison, WI) for lateral positioning. The SICM was operated in bias modulated (BM) mode,[47] in which there was zero net bias between the two QRCEs. A lock-in amplifier (SR830, Stanford Research Systems, Sunnyvale, CA) was used to generate an oscillating bias (38 mV amplitude, 357 Hz frequency) applied to the bulk QRCE, and the resulting current was measured at the QRCE in the nanopipette using a custom-built wideband current-to-voltage converter. The instrument was controlled and data collected with a programmed FPGA card (7852R, National Instruments, Austin, TX) using LabVIEW (2013, National Instruments, Austin TX).

The experimental configuration for optical and SICM dissolution measurements is illustrated in Figure 1. Furosemide crystals, typically with the longest dimension ranging from 30 - 60 μm and various length-width-height ratios, were selected. Some crystals were removed to create separations greater than 40× times their largest dimension to ensure high undersaturation (sink conditions) and avoid overlap of diffusion profiles among neighboring crystals. Following addition of 4 mL of a 50 mM aqueous solution of KCl to the Petri dish, time-lapse sequence of optical images (400× magnification, every 30 s) and line traces along the crystal in an SICM hopping mode[48,49] were acquired. The nanopipette probe was lowered toward the surface at a rate of 1 μm s^{-1} at each position. When the surface was detected by the probe as a change in the phase of the AC current to a defined set point (typically 0.1° change from the bulk phase value), the z position was recorded and the nanopipette was retracted 5 μm at a rate of 10 μm s^{-1}, after which it was moved laterally to a new location, typically 3-6 μm from the previous position. This process was then repeated at a minimum of 10 lateral positions, which enabled acquisition of line profile and

measurement of crystal height in approximately 60 seconds. Crystal dimensions were determined from the optical microscope images using ImageJ (version 1.45, NIH).

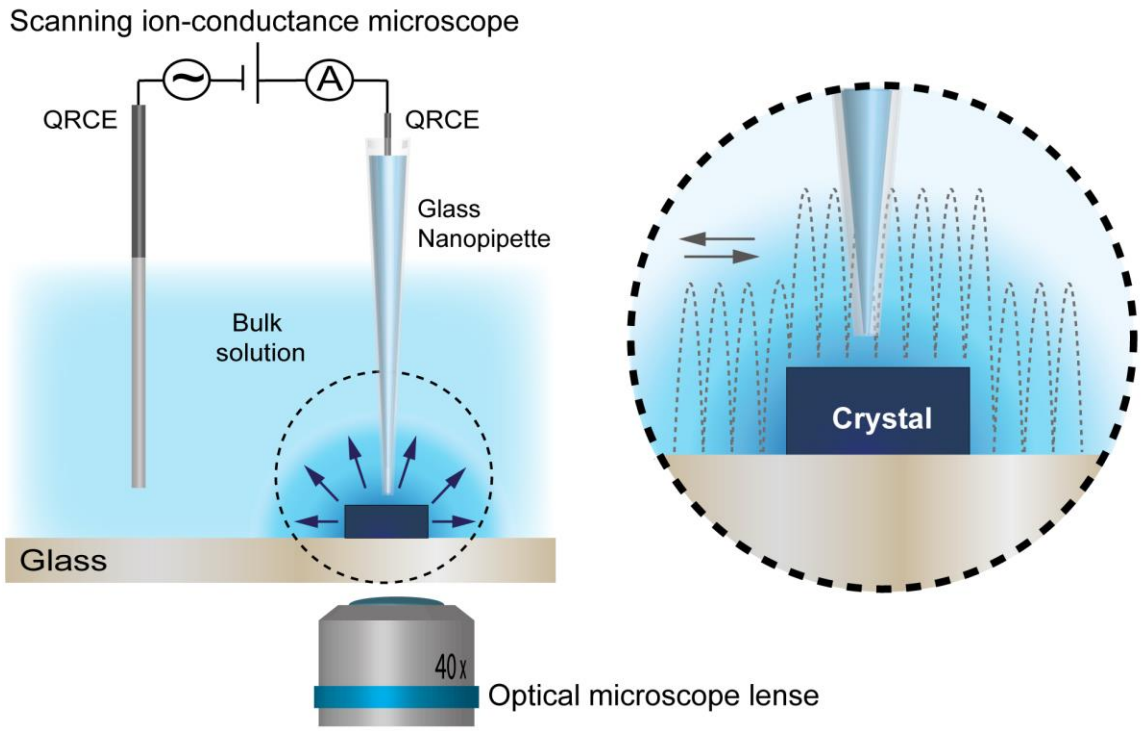

Figure 1. Optical microscopy–SICM configuration. The SICM system was mounted on an inverted optical microscope for the simultaneous tracing of the dissolution process by optical microscopy and SICM. The petri dish containing the crystals was positioned on the microscope stage and the nanopipette for SICM scans was submerged normal to the surface. Line traces of the local height along the crystal were generated in hopping mode BM-SICM, with the probe scanned forward and backward over the same line along the crystal (right).

Atomic Force Microscopy (AFM). AFM images of furosemide crystals mounted on the glass slide in the Petri crystallization dish were acquired in air before and after partial dissolution using a BioScope Catalyst microscope (Bruker, Billerica, MA). Crystals separated by >10 times the largest crystal dimension were allowed to dissolve partially after addition of 4 mL of 50 mM aqueous solution of KCl to the petri dish for 10 minutes. The electrolyte solution was then removed and the partially dissolved crystals were rinsed quickly with DI water and dried with a nitrogen stream. AFM images were acquired in the *ScanAsyst mode* using triangular-shaped silicon nitride cantilevers (SNL-10, Bruker, Billerica, MA) with a resonant frequency of ~65 kHz and ~0.35 N/m spring constant and a data collection resolution of

512 points per raster line. The images were analyzed with SPIP software (6.0.14, Image Metrology, Denmark).

Simulations. Numerical simulations were performed using the commercial finite element method package Comsol Multiphysics 4.4 (Comsol AB, Sweden) installed on a Dell Intel Core 7i Quad 2.93 GHz computer equipped with 16 GB of RAM running Windows 7 Professional 64 bit. The "mass transport of diluted species" module was used in the 3D domain illustrated in Figure 2.

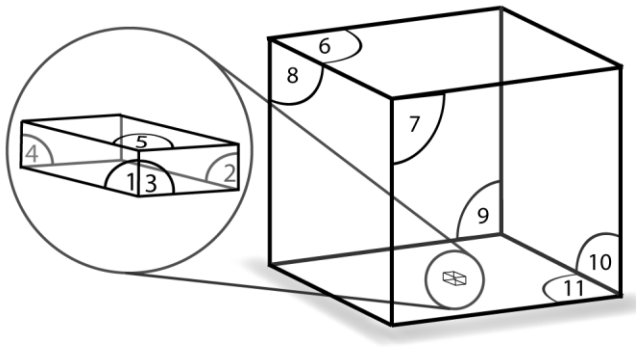

Figure 2. Three-dimensional domain used for FEM simulations (not drawn to scale). The numbers correspond to the boundaries described in Table 1.

The maximum characteristic diffusional time for mass transport from microscopic surfaces to bulk solution can be estimated using a semi-infinite diffusion model according to equation 1, where t_{diff} is the steady-state diffusion time, d is crystal largest dimension size and D denotes diffusion coefficient.

$$t_{diff} \approx d^2 / D \qquad (1)$$

The diffusion coefficient of furosemide was estimated from the Wilke-Chang correlation[50] (6.15×10^{-6} cm^2/s) and was assumed constant over the entire domain. The diffusion time for a dissolving crystal of $d \sim$ 45 μm is about 3 seconds, three orders of magnitude faster than the duration of a typical crystal dissolution experiment (30 minutes for the complete dissolution of a crystal). The influence of convection was neglected due to the small nature of the studied crystals (largest dimension < 60 μm).[51] Mass transport by diffusion was therefore assumed to be effectively at a steady-state, such that the flux conservation relation in equation 2 was valid, where J is the flux, c is the concentration of the furosemide solute, and D is the furosemide diffusion coefficient.

$$\nabla J = -D\nabla^2 c = 0 \qquad (2)$$

The model, denoted here M1, was developed by applying a flux (per unit area) for each crystal face (observed dissolution rate, $J_{(hkl)}^{Obs}$) measured experimentally. Using the appropriate boundary conditions (Table 1) the concentration of furosemide in the solution around the dissolving crystal could be simulated, from which it was possible to distinguish the dissolution regime, i.e., mass transport *vs*. kinetic control; *vide infra*. In order to deduce the relative importance of mass transport and surface kinetics, a model (M2) with the same geometry but different boundary conditions was employed (Table 1), such that dissolution was controlled by diffusion (crystal/solution interface saturated). Solution of the partial differential equations for both models (M1 and M2) was achieved using the direct solver MUMPS in the COMSOL environment, with a relative error tolerance of 10^{-6}. Simulations were carried out with >7,500,000 tetrahedral mesh elements. The mesh resolution was refined to be the finest, down to a value of 0.1 nm, at the surfaces of the crystal.

Table 1. Boundary conditions for numerical simulations of furosemide crystal dissolution

Boundary	**Characteristics**	**Boundary conditions** M1	**Boundary conditions** M2
1, 2	Crystal faces {010}	$J_{(hkl)}^{Obs} = -\mathbf{n}\cdot(D\nabla c)$	$c = c_s$
3, 4	Crystal faces {101}	$J_{(hkl)}^{Obs} = -\mathbf{n}\cdot(D\nabla c)$	$c = c_s$
5	Crystal face (001)	$J_{(hkl)}^{Obs} = -\mathbf{n}\cdot(D\nabla c)$	$c = c_s$
6, 7, 8, 9, 10	Bulk solution	$c = c_0 = 0$	$c = c_0 = 0$
11	Glass slide	$0 = -\mathbf{n}\cdot(D\nabla c)$	$0 = -\mathbf{n}\cdot(D\nabla c)$

The boundary numbers are for the planes labeled in Figure 2

n denotes the vector normal to the surface

c_s is the solubility concentration of furosemide (0.2 mM)

RESULTS AND DISCUSSION

Furosemide crystals. Four polymorphic forms and two solvates of furosemide have been reported previously.[37,52,53] The investigation described herein focused on Polymorph I, which is the only polymorph present in the commercial drug.[53] Single crystal CCD X-ray diffraction confirmed that recrystallized furosemide crystals were polymorph I, which crystallizes in the triclinic P-1 space group (see Supporting Information Table S1).[37] Powder X-ray diffraction of furosemide crystals grown on a glass slide from ethanol/water solutions supersaturated with furosemide revealed only peaks corresponding to the (*00l*) reflections (*l* = 1 - 3), confirming that the crystals were oriented with the (001) face parallel to the glass slide (Supporting Information, Figure S1). Optical microscopy revealed a raft-like habit with a triclinic morphology (Figure 3A, B).

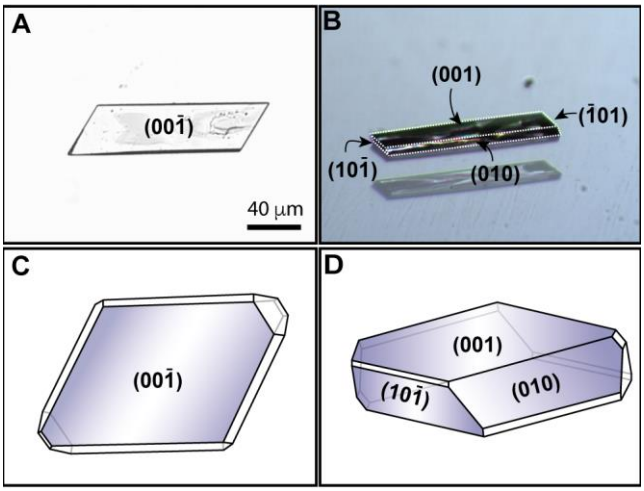

Figure 3. Morphology of a typical recrystallized furosemide crystal (Polymorph I). The different faces that can be seen are labeled. (A) Image acquired with an optical microscope, normal to the (00$\bar{1}$) face. (B) Optical image acquired with a magnifying CCD camera in an SICM experiment (the lighter image is the reflection of the actual crystal in the glass slide). (C) Habit of furosemide Polymorph I calculated using the growth morphology method, viewed normal to the (00$\bar{1}$) face. (D) Calculated habit of furosemide Polymorph I oriented to reveal other major crystal faces.

Crystal morphology prediction can serve as a useful aid in identifying relevant crystal faces when crystal dimensions are less than those required for indexing by X-ray diffraction. Methods for predicting crystal morphology based on crystal structure have become routine and yield crystal morphologies that are consistent with experimental morphologies for a wide range of molecular crystals despite a lack of consideration for the external growth environment.[54] These methods include (*i*) the Bravais-Friedel

Donnay-Harker (BFDH), a geometric calculation based on crystal lattice and symmetry; (*ii*) the equilibrium method, based on the surface free energies of relevant crystal faces; and (*iii*) the growth (or "attachment energy") method, based on attachment energies corresponding to relevant crystal faces. The growth method (*iii*) is most effective when considering only the internal interactions of the crystal structure.[55-56] The growth method, developed by Hartmann and Perdok, relies on the bond energy released when one building unit is attached to the surface of a crystal face to predict crystal morphology.[57,58] The growth rate normal to a particular face is proportional to the attachment energy for that surface — large attachment energies (*i.e.* more negative values) for a specific face correspond to strong out-of-plane intermolecular interactions, corresponding to faster growth normal to the plane and a lower morphological significance for the face.

Three force fields that have been used often for the prediction of organic crystals habits[59-61] were evaluated for predicting the morphology of furosemide Polymorph I. The molecular geometries and lattice parameters of the furosemide unit cell were optimized using the COMPASS, Dreiding, and cvff forcefields (see Supporting Information Table S2). The COMPASS forcefield was chosen for morphology calculations because it provided the lowest lattice energy and the lattice parameters best matched those of the experimental unit cell. The furosemide morphology predicted from the COMPASS forcefield reveals that three crystal faces — (001), (010) and $(10\bar{1})$ — contribute to 90% of the predicted total area of the crystal (Figure 3C, D; Table 2). Crystal faces with a calculated area of <5% were not observed in the experimental morphology, which is not surprising given that experimental crystal habit is strongly affected by many environmental factors, including solvent, supersaturation, pH, and temperature,[59,62] which are not captured in the morphology prediction calculations. These crystal faces, if present, cannot be studied by the measurements conducted in our experiments and are not addressed here.

Table 2. Morphology predictions for the optimized structure of furosemide (Polymorph I) by growth morphology calculations using COMPASS force field.

Face *(hkl)*	d_{hkl} (Å)	E_{att} (kcal mol^{-1})	Total facet area (%)
(0 0 1)	13.854	-33.917	53.16
(0 1 0)	9.021	-78.355	18.15
(1 0 $\bar{1}$)	8.613	-79.740	18.82
(0 1 $\bar{1}$)	8.469	-87.333	3.44
(1 0 0)	8.411	-94.402	1.81
(1 $\bar{1}$ 0)	8.365	-124.774	4.02
(1 $\bar{1}$ $\bar{1}$)	7.626	-124.298	0.59

Determination of dissolution rates and interfacial concentrations. Since the introduction of SICM,[34] different modes such as constant distance,[35] hopping approach,[49] and hybrid[63] have been used to acquire images of the topography of soft surfaces[36, 64] and for local ion current measurements.[65-67] Most recently, a new method based on the application of an oscillating bias between both QRCEs to generate an alternating ion current (AC) feedback signal, bias modulated SICM (BM─SICM),[47] has been introduced. This approach has several advantages over the traditional nanopipette oscillation SICM method, including minimization of perturbations of the local ionic atmosphere and from effects of convection (stirring) and electro-osmosis. Moreover, it offers opportunities for faster imaging.[67]

The dissolution rate is expected to be determined by a combination of (*i*) interfacial (intrinsic) dissolution kinetics, which are governed by energetics of the surface and solvation effects, and (*ii*) mass transport of dissolved species from the crystal surface to the bulk solution.[18] Consequently, dissolution kinetics reflects a competition between these two processes, with the slowest governing the overall rate, leading to either kinetic (interfacial) control, mass transport (diffusion) control, or a mixed regime where both contributions are comparable. The measurement of intrinsic dissolution kinetics requires the mass transport rates to be comparable to or greater than surface kinetics, which in turn requires that mass transport is well defined and calculable.

The temporal change in the lateral dimensions of furosemide crystals (i.e. the size of the (001) face) was recorded by measurement of the retreat of the {010} and {101} faces using optical microscopy (Figure 4A). The changes in crystal height (normal to the (001) face) were obtained by BM-SICM for the (001) face (Figure 4B, D). Collectively, these measurements identify the change in crystal size for all three dimensions. The dissolution rate was effectively constant for all three faces during the first ten minutes, but at longer times the dissolution rate increased. The faster dissolution rate was accompanied by surface roughening and the formation of pits on the (001) surface (*vide infra*), which were evident even in optical images. It is reasonable to suggest that the roughened surfaces and pits would result in higher index microfacets in the crystal surface, leading to enhanced dissolution kinetics (Figure 4A). Under these conditions, it is anticipated that crystal dissolution becomes increasingly limited by mass transport.[28,68-70] This is consistent with our recent observation of the dissolution kinetics of the (110) face of salicylic acid in aqueous solution using hopping intermittent contact-scanning electrochemical microscopy,[70] where we found a strong influence of surface roughness on the dissolution kinetics.

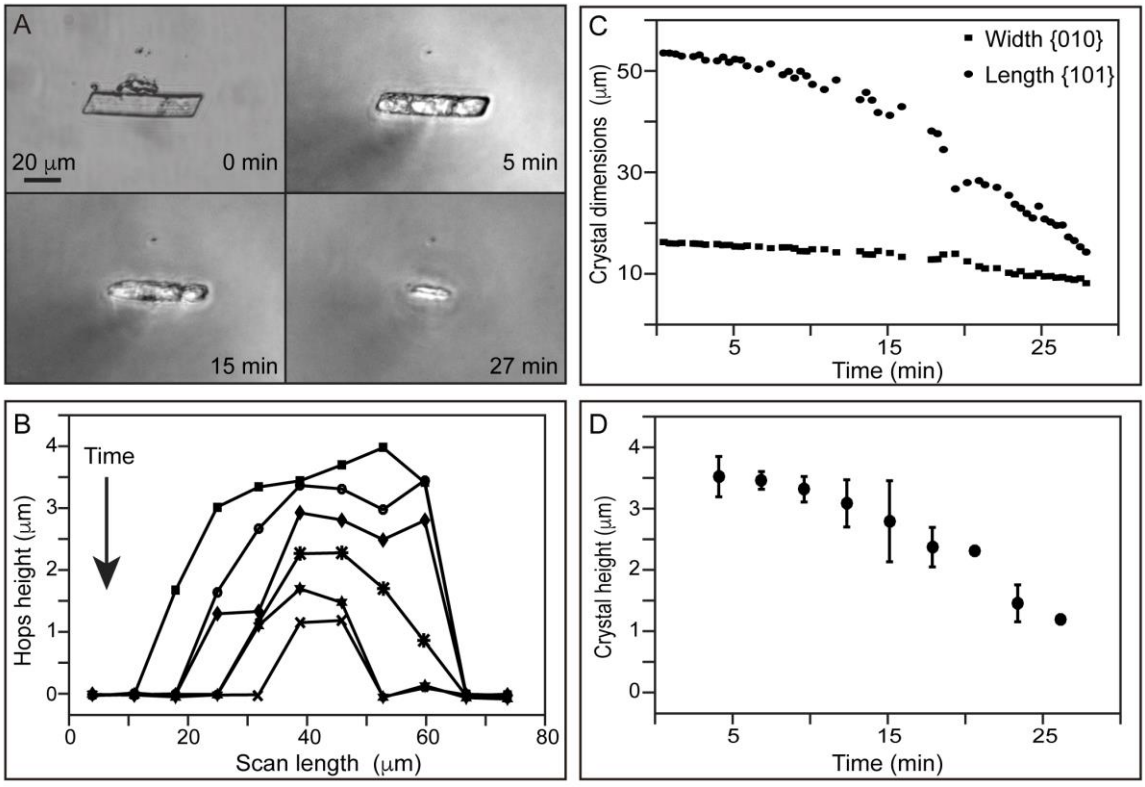

Figure 4. (A) Representative time-lapse optical microscopy images of the dissolution of a furosemide crystal. (B) BM-SICM line scans recorded at : 4 (■), 10 (•), 15 (♦), 20 (✱), 23 (✸) and 26 (✖) minutes after the beginning of dissolution. (C) Retreat of the {010} and {101} faces (length and width dimensions) over time. (D) Reduction of the crystal height during dissolution, plotted as an average value of all the hops landed on the crystal surface in a SICM line scan.

The early stage of dissolution, where the rate was constant, was investigated for nine furosemide crystals in order to compare the initial dissolution rates for the three crystallographically unique crystal faces. In this regime the dissolution rates likely correspond to the kinetic processes at the low index faces rather than the higher index microfacets that define the pitted surface. The rates of dissolution ($J^{Obs}_{(hkl)}$) were determined using equation 3, where $v_{(hkl)}$ is the dissolution velocity of face *hkl* and $V_{mcrystal}$ is the molar volume of furosemide (200.692 cm^3/mol, calculated from the density of polymorph I, 1.648 g/cm^3). The standard deviation of the $J^{Obs}_{(hkl)}$ values is rather large, which can be attributed to the small sample size, the use of crystals with slightly different dimensions, and mixed kinetic-mass transport control (*vide infra*). Nonetheless, it is evident that the different faces exhibit different dissolution rates, with $J^{Obs}_{(hkl)}$ increasing in the order (001) < (010) < $(10\bar{1})$, inversely proportional to the areas of the faces.

$$J^{Obs}_{(hkl)} = v_{(hkl)} / V_{m\,crystal} \qquad (3)$$

Table 3. Average face-resolved initial dissolution rates of 9 furosemide crystals**.**

Face (*hkl*)	J^{Obs} (mol m^{-2} s^{-1})
$(10\bar{1})$	$(16.1 \pm 6.7) \times 10^{-6}$
(010)	$(12.6 \pm 6.9) \times 10^{-6}$
(001)	$(2.8 \pm 1.4) \times 10^{-6}$

Crystallographically unique faces of a molecular crystal will have different chemical compositions and molecular topography. Consequently, different interactions with the external environment can be expected for these faces,[71] as well as different step/kink energetics. The dissolution rates of crystal faces depend on the energetics associated with each surface. The lowest energy surfaces are those in which the weakest bonds are truncated. In the furosemide crystal, each molecule participates in six hydrogen bonds with five neighboring furosemide molecules — one O···HO, one OH···O, two NH···O, and two O···HN (Scheme 2), forming a complex hydrogen-bonding network that is truncated differently at each of the morphologically significant (001), (010), and $(10\bar{1})$ faces (Figure 5). The (001) face presents furanyl rings, which do not form hydrogen bonds with other furosemide molecules, to the external environment. Moreover, the hydrogen bonding network is contained within the (001) plane such that hydrogen bonds

are not truncated at the surface and in-plane interactions are strong, characteristic of a face with low surface energy, slow growth, and a large morphological importance (Figure 5A). In contrast, the (010) and $(10\bar{1})$ surfaces expose aminosulfonyl and carboxyl groups at the surface, thereby truncating the hydrogen-bonding network (Figure 5B, C). Based on this structural inspection alone, the (001) face would be expected to have a lower attachment energy than the (010) and $(10\bar{1})$ faces and should have the slowest growth rate normal to the surface, and be the slowest dissolving crystal face as well. This is consistent with the observed and calculated crystal morphology (Figure 3 and Table 2), as well as the measured dissolution rates (Table 3). The comparable morphological significance of (010) and $(10\bar{1})$ suggests that these surfaces have comparable growth and dissolution rates. The $(10\bar{1})$ face, however, exhibits a somewhat higher dissolution rate compared to (010), although the two are comparable within error. The corrugation of the (010) face suggests that solvent ordering or surface reconstruction may be likely, which would stabilize this face and slow its dissolution rate compared to the relatively flat $(10\bar{1})$ face.[72] Nonetheless, the order of the observed dissolution rates of the different furosemide crystal faces (001) < (010) < $(10\bar{1})$ agrees with the hydrogen bonding model as well as the attachment energy calculations. This trend becomes even clearer when mass-transport corrections are introduced (*vide infra*).

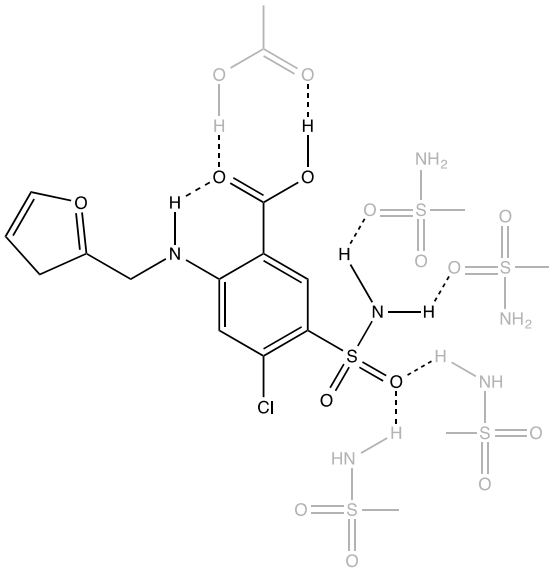

Scheme 2. The molecular structure of furosemide (black) and hydrogen bonds formed by each molecule with neighboring furosemide molecules (grey) in the crystal structure.

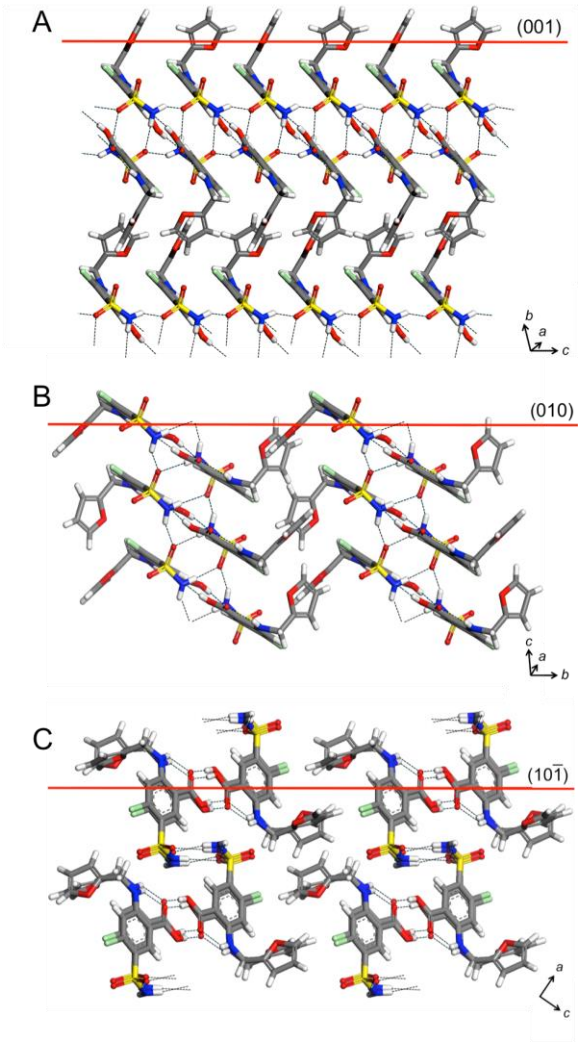

Figure 5. Structure of furosemide crystal faces: (A) (001), (B) (010), and (C) (10$\bar{1}$). Black dotted lines represent hydrogen bonds.

Mass transport-corrected intrinsic dissolution kinetics. FEM models were formulated for each of the nine crystals studied to obtain more insight into the dissolution kinetics, particularly the role of mass transport. These computations accounted for the experimental dissolution rate ($J_{(hkl)}^{Obs}$) obtained for each individual crystal face, crystal size and crystal morphology, thereby producing the concentration distribution and diffusive flux of furosemide. The results from FEM modeling of the dissolution of four representative furosemide crystals are provided in Figure 6. The calculations reveal that the concentration of furosemide at the solid/liquid interface is higher than in the bulk solution, with large concentration gradients (diffusion layer) between the crystal and the bulk solution, consistent with significant contributions from mass transport. Notably, the calculated concentration in the vicinity of each crystal

face differs, demonstrating that the balance between mass transport and surface kinetics for each crystal face during the dissolution process is different. The calculated surface concentrations increase in the order $C_{(001)}$ = 0.12 ± 0.04 mM < $C_{(010)}$ = 0.15 ± 0.04 mM < $C_{(10\bar{1})}$ = 0.17 ± 0.03 mM, consistent with the order of faster kinetics expected and a trend towards an increased degree of mass transport control. The contribution of surface kinetics is important on those faces where the interfacial concentration is less than the solubility of furosemide (0.2 mM),[73] a value that was confirmed by UV–Vis absorption (Supporting Information, Figure S2). The interfacial concentration alone, however, is not indicative of dissolution kinetics due to the possible redistribution of the solute between the different crystal faces, which depends on the direction and magnitude of the diffusive flux of material, crystal size and morphology. A more accurate quantitative determination of the contribution of the surface kinetics ($J^{SK}_{(hkl)}$) can be obtained for each crystal face by comparing the experimental flux ($J^{Obs}_{(hkl)}$) determined in model M1 (see Experimental Section), with the value of the theoretical diffusive flux on each crystal face predicted from simulations for a pure mass transport controlled system ($J^{MT}_{(hkl)}$) parameterized with the same crystal geometry (model M2). The overall flux involves mass transport and surface kinetics in series, according to equation 4,

$$\frac{1}{J^{Obs}_{(hkl)}} = \frac{1}{J^{MT}_{(hkl)}} + \frac{1}{J^{SK}_{(hkl)}} \qquad (4)$$

$J^{Obs}_{(hkl)}$ for (010) and $(10\bar{1})$ was very close to $J^{MT}_{(hkl)}$ ($J^{Obs}_{(hkl)} \approx J^{MT}_{(hkl)}$), consistent with fast surface dissolution kinetics ($J^{SK}_{(hkl)} >> J^{MT}_{(hkl)}$). Conversely, for the (001) face, except for one crystal (among the nine) that could not be distinguished from mass-transport control, $J^{Obs}_{(hkl)}$ was always much smaller than $J^{MT}_{(hkl)}$ ($J^{Obs}_{(hkl)} << J^{MT}_{(hkl)}$), consistent with mixed kinetic control ($J^{SK}_{(hkl)} \approx J^{MT}_{(hkl)}$). For the (001) face, the average value of $J^{MT}_{(hkl)}$ for the range of crystals shown (7.35×10^{-6} mol m^{-2} s^{-1}) is about twice the size of the average value of $J^{SK}_{(hkl)}$ (4.39×10^{-6} mol m^{-2} s^{-1}). It is important to note, however, that a range in values was obtained for $J^{Obs}_{(hkl)}$, $J^{MT}_{(hkl)}$ and $J^{SK}_{(hkl)}$ across the different crystals studied. This is attributed to the different numbers of defects in each crystal and the different crystal sizes. The average values for each flux contribution for each crystal face are provided in Table 4 (more detail is provided in Supporting Information Table S3).

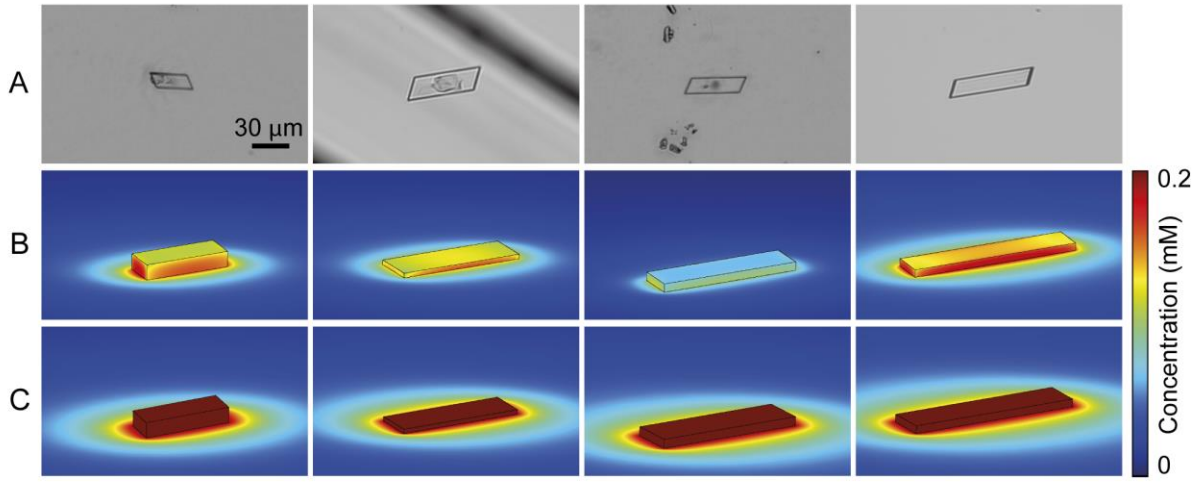

Figure 6. A) Optical microscopy images of single furosemide crystals. B) Results of FEM simulations (M1) for the concentration distribution of furosemide during the dissolution. C) Concentration distribution of furosemide in the solid/liquid interface in a mass transport controlled dissolution process (M2).

Table 4. Average diffusive fluxes per unit area for each crystal face calculated from FEM simulations of eight furosemide crystals.

Face (hkl)	J_{Obs} (mol m^{-2} s^{-1})	J_{MT} (mol m^{-2} s^{-1})	J_{SK} (mol m^{-2} s^{-1})
$(10\bar{1})$	$(16.1 \pm 6.7) \times 10^{-6}$	$(15.0 \pm 4.9) \times 10^{-6}$	Near diffusion control
(010)	$(12.6 \pm 6.9) \times 10^{-6}$	$(11.7 \pm 3.6) \times 10^{-6}$	Near diffusion control
(001)	$(2.8 \pm 1.4) \times 10^{-6}$	$(7.4 \pm 1.8) \times 10^{-6}$	$(4.4 \pm 2.7) \times 10^{-6}$

Dislocations are recognized to be important for etch pit formation during dissolution.[74] Pitting leads to both an increase in the specific surface area and the formation of microdomains (pit walls) of higher surface energy that produces an increased dissolution rate.[70] In the case of furosemide crystals, a collection of crystals was examined by AFM before and after their immersion in aqueous solution for 10 minutes (Figure 7). Prior to dissolution the (001) surfaces are largely free of defects, except for crystal C, which appears to be somewhat rough based on an AFM line profile (red line in Figure 7C). After simultaneous immersion for 10 minutes, the crystals have dissolved, although to different extents. Moreover, the number and depth of pits on the (001) face differ for each crystal. It can be appreciated in the images that the extent of dissolution depends on the initial crystal size, the ratio of the size of the (010) and $(10\bar{1})$ faces, and the initial surface roughness. Overall, the smaller the crystal, and the smaller

the size of the $(10\bar{1})$ face in relation to the (010) face, and the rougher the crystal surface, the faster the dissolution. All these characteristics are united in crystal C which is the smallest crystal (37 µm length), has a small $(10\bar{1})$ face and the clear presence of a defect on the (001) surface (surface roughness profile in red in Figure 7) prior to dissolution. After 10 minutes, crystal C has dissolved by *ca.* 70 % from its initial volume, while the other crystals have dissolved by between 45 % and 60 %. Differences in the pitting density (surface area and roughness) are evident in the images after dissolution and the surface roughness plot in Figure 7. The (001) surface of the dissolved crystals A and B is characterized by a smaller proportion of pits than crystals C and D. After the 10 minute dissolution period, the decrease in crystal size, as well as the roughening of the crystal faces exposed to the solvent by the formation of pits and exposure of high index faces, explains the increased dissolution kinetics at longer times (Figure 4).

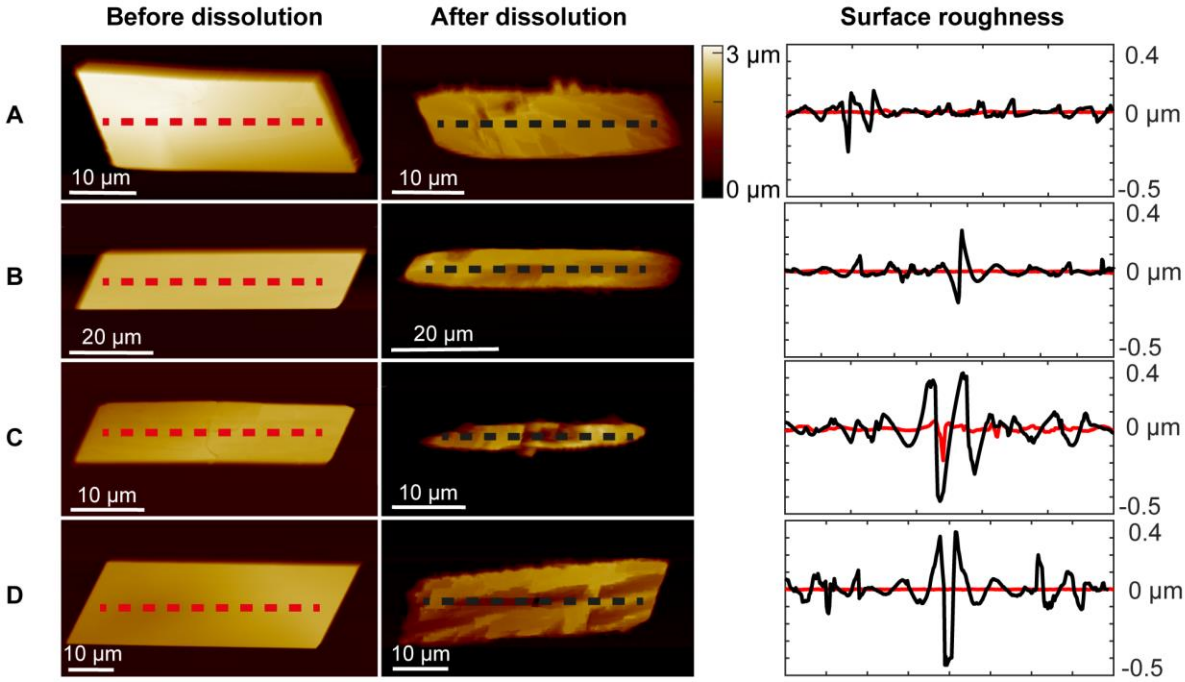

Figure 7. AFM images of single furosemide crystals before dissolution and after partial dissolution for 10 minutes. The dashed red and black lines indicate the line profile used to measure the surface roughness before and after dissolution respectively (left). Surface roughness (right) of the (001) face in each of the four crystals before dissolution (red) and after partial dissolution (black).

CONCLUSIONS

The dissolution kinetics of the individual faces of single furosemide crystals (polymorph I) have been investigated by a versatile *in situ* multimicroscopy approach, comprising SICM and optical microscopy combined with finite element method (FEM) modeling. The experimental approach allowed 3D visualization of crystal morphology during dissolution, from which a numerical model was developed to calculate the concentration distribution around the crystal and dissolution flux of furosemide at the solid/liquid interface. This allowed the quantitative comparison of mass transport and surface kinetics. It has been shown that the (001) face is strongly influenced by surface kinetics (mixed kinetic control), while the (010) and $(10\bar{1})$ faces are dominated by mass transport. Our findings have important consequences for the reporting of dissolution kinetics: dissolution rates vary considerably from crystal to crystal and are time dependent at large dissolution times (>10 minutes). This is due to the impact of a range of factors, including subtle effects from crystal size, shape and the apparent number of defects (pits) in a particular crystal, and as shown by complementary AFM measurements. By studying individual microscale crystals within a population, we have been able to identify kinetic distributions for individual faces and rationalize the results in terms of crystal structure and surface properties. The ability to obtain this quantitative information for individual crystal faces suggests a pathway to understanding crystal dissolution at the molecular level that can be used to tailor crystal morphology to enhance dose-release properties and regulating bioavailability. More generally, the proposed approach should be widely applicable to a range of crystal types, encompassing organic and ionic crystals.

ACKNOWLEDGEMENTS

This work was supported by the European Research council (ERC-2009-AdG247143-QUANTIF), Marie Curie Initial Training Network FP7-PEOPLE-2012_ITN Grant Agreement Number 31663 CAS-IDP (M.A-V.), Marie Curie IntraEuropean Fellowship 626158 FUNICIS (D.M.) and AstraZeneca (F.M.M). The NYU authors acknowledge the support of the MRSEC Program of the National Science Foundation under Award Number DMR-1420073, the GOALI program of the National Science Foundation under award DMR-1206337, and the NSF CRIF Program (CHE-0840277) for shared facilities. L.N.P is also grateful to the New York University Department of Chemistry for a Margaret and Herman Sokol Predoctoral Fellowship.

SUPPORTING INFORMATION DESCRIPTION

Crystallographic parameters of furosemide polymorph I, comparison of calculated and experimental PXRD patterns of furosemide polymorph I, comparison of the optimized furosemide unit cell parameters and single crystal CCD X-ray diffraction data, UV-Vis spectra of furosemide dissolved in water at different concentrations and detailed list of finite element method simulation results for each analyzed crystal.

REFERENCES

1. Chen, J.; Sarma, B.; Evans, J. M. B.; Myerson, A. S. *Cryst. Growth Des.* **2011**, *11*, 887-895.

2. Vippagunta, S. R.; Brittain, H. G.; Grant, D. J. W. *Adv. Drug Delivery Rev.* **2001**, *48*, 3-26.

3. Blagden, N.; de Matas, M.; Gavan, P. T.; York, P. *Adv. Drug Delivery Rev.* **2007**, *59*, 617-630.

4. Fan, C.; Chen, J.; Chen, Y.; Ji, J.; Teng, H. H. *Geochim. Cosmochim. Acta* **2006**, *70*, 3820-3829.

5. York, P. *Int. J. Pharm.* **1983**, *14*, 1-28.

6. Hörter, D.; Dressman, J. B. *Adv. Drug Delivery Rev.* **2001**, *46*, 75-87.

7. Byrn, S. R.; Pfeiffer, R. R.; Stowell, J. G. *Solid-state chemistry of drugs*; SSCI, Inc.: West Lafayette, Ind., 1999.

8. Carter, P. W.; Ward, M. D. *J. Am. Chem. Soc.* **1993**, *115*, 11521-11535.

9. Carter, P. W.; Hillier, A. C.; Ward, M. D. *J. Am. Chem. Soc.* **1994**, *116*, 944-953.

10. Vekilov, P. G.; Monaco, L. A.; Rosenberger, F. *J. Cryst. Growth* **1995**, *148*, 289-296.

11. Vekilov, P. G.; Ataka, M.; Katsura, T. *J. Cryst. Growth* **1993**, *130*, 317-320.

12. Malkin, A. J.; Kuznetsov, Y. G.; McPherson, A. *J. Cryst. Growth* **1999**, *196*, 471-488.

13. Van Driessche, A. E. S.; Otálora, F.; Sazaki, G.; Sleutel, M.; Tsukamoto, K.; Gavira, J. A. *Cryst. Growth Des.* **2008**, *8*, 4316-4323.

14. Michaels, A. S.; Colville, A. R. *J. Phys. Chem.* **1960**, *64*, 13-19.

15. Jouyban-Gharamaleki, A.; Dastmalchi, S.; Chan, H.-K.; Hanaee, J.; Javanmard, A.; Barzegar-Jalali, M. *Drug Dev. Ind. Pharm.* **2001**, *27*, 577-583.

16. Pabla, D.; Akhlaghi, F.; Zia, H. *Eur. J. Pharm. Biopharm.* **2009**, *72*, 105-110.

17. Jeschke, A. A.; Vosbeck, K.; Dreybrodt, W. *Geochim. Cosmochim. Acta* **2001**, *65*, 27-34.

18. Unwin, P. R.; Macpherson, J. V. *Chem. Soc. Rev.* **1995**, *24*, 109-119.

19. Sjöberg, E. L.; Rickard, D. *Geochim. Cosmochim. Acta* **1983**, *47*, 2281-2285.

20. Sherwood, T. K.; Pigford, R. L.; Wilke, C. R. *Mass transfer*; McGraw-Hill, 1975.

21. Unwin, P. R.; Barwise, A. J.; Compton, R. G. *J. Colloid Interface Sci.* **1989**, *128*, 208-222.

22. Mbogoro, M. M.; Snowden, M. E.; Edwards, M. A.; Peruffo, M.; Unwin, P. R. *J. Phys. Chem. C* **2011**, *115*, 10147-10154.

23. Danesh, A.; Connell, S. D.; Davies, M. C.; Roberts, C. J.; Tendler, S. J. B.; Williams, P. M.; Wilkins, M. J. *Pharm Res* **2001**, *18*, 299-303.

24. Guo, S.; Ward, M. D.; Wesson, J. A. *Langmuir* **2002**, *18*, 4284-4291.

25. Li, T.; Morris, K. R.; Park, K. *J. Phys. Chem. B* **2000**, *104*, 2019-2032.

26. Abendan, R. S.; Swift, J. A. *Cryst. Growth Des.* **2005**, *5*, 2146-2153.

27. Perry, A. R.; Peruffo, M.; Unwin, P. R. *Cryst. Growth Des.* **2013**, *13*, 614-622.

28. Prasad, K. V. R.; Ristic, R. I.; Sheen, D. B.; Sherwood, J. N. *Int. J. Pharm.* **2002**, *238*, 29-41.

29. Macpherson, J. V.; Unwin, P. R. *Prog. React. Kinet.* **1995**, *20*, 185-244.

30. Macpherson, J. V.; Unwin, P. R. *J. Phys. Chem.* **1994**, *98*, 1704-1713.

31. Kinnear, S. L.; McKelvey, K.; Snowden, M. E.; Peruffo, M.; Colburn, A. W.; Unwin, P. R. *Langmuir* **2013**, *29*, 15565-15572.

32. Shekunov, B. Y.; Grant, D. J. W. *J. Phys. Chem. B* **1997**, *101*, 3973-3979.

33. Hiroshi, K.; Satoru, M.; Yoshihisa, S. *Jpn. J. Appl. Phys.* **1993**, *32*, L1855.

34. Hansma, P. K.; Drake, B.; Marti, O.; Gould, S. A.; Prater, C. B. *Science* **1989**, *243*, 641-643.

35. Shevchuk, A. I.; Frolenkov, G. I.; Sanchez, D.; James, P. S.; Freedman, N. *Angew. Chem. Int. Ed. Engl.* **2006**, *45*, 2212-2216.

36. Chen, C.-C.; Zhou, Y.; Baker, L. A. *Annu. Rev. Anal. Chem.* **2012**, *5*, 207-228.

37. Babu, N. J.; Cherukuvada, S.; Thakuria, R.; Nangia, A. *Cryst. Growth Des.* **2010**, *10*, 1979-1989.

38. Nielsen, L. H.; Gordon, S.; Holm, R.; Selen, A.; Rades, T.; Müllertz, A. *Eur. J. Pharm. Biopharm.* **2013**, *85*, 942-951.

39. Murray, M. D.; Haag, K. M.; ́black, P. K.; Hall, S. D.; Brater, D. C. *Pharmacotherapy* **1997**, *17*, 98-106.

40. Pudipeddi, M.; Serajuddin, A. T. M. *J. Pharm. Sci.* **2005**, *94*, 929-939.

41. Ai, H.; Jones, S. A.; de Villiers, M. M.; Lvov, Y. M. *J. Controlled Release* **2003**, *86*, 59-68.

42. Garnero, C.; Chattah, A. K.; Longhi, M. *Carbohydr. Polym.* **2013**, *94*, 292-300.

43. Menon, A.; Ritschel, W. A.; Sakr, A. *J. Pharm. Sci.* **1994**, *83*, 239-245.

44. Dolomanov, O. V.; Bourhis, L. J.; Gildea, R. J.; Howard, J. A. K.; Puschmann, H. *J. Appl. Crystallogr.* **2009**, *42*, 339-341.

45. Sheldrick, G. *Acta Crystallogr., Sect. A: Found. Adv.* **2008**, *64*, 112-122.

46. Nadappuram, B. P.; McKelvey, K.; Al Botros, R.; Colburn, A. W.; Unwin, P. R. *Anal. Chem.* **2013**, *85*, 8070-8074.

47. McKelvey, K.; Perry, D.; Byers, J. C.; Colburn, A. W.; Unwin, P. R. *Anal. Chem.* **2014**, *86*, 3639-3646.

48. Novak, P.; Li, C.; Shevchuk, A. I.; Stepanyan, R.; Caldwell, M.; Hughes, S.; Smart, T. G.; Gorelik, J.; Ostanin, V. P.; Lab, M. J.; Moss, G. W. J.; Frolenkov, G. I.; Klenerman, D.; Korchev, Y. E. *Nat. Methods* **2009**, *6*, 279-281.

49. Yang, X.; Liu, X.; Zhang, X.; Lu, H.; Zhang, J.; Zhang, Y. *Ultramicroscopy* **2011**, *111*, 1417-1422.

50. Wilke, C. R.; Chang, P. *AIChE J.* **1955**, *1*, 264-270.

51. Amatore, C.; Pebay, C.; Thouin, L.; Wang, A.; Warkocz, J. S. *Anal. Chem.* **2010**, *82*, 6933-6939.

52. Matsuda, Y.; Tatsumi, E. *Int. J. Pharm.* **1990**, *60*, 11-26.

53. Goud, N. R.; Gangavaram, S.; Suresh, K.; Pal, S.; Manjunatha, S. G.; Nambiar, S.; Nangia, A. *J. Pharm. Sci.* **2012**, *101*, 664-680.

54. Docherty, R.; Clydesdale, G.; Roberts, K. J.; Bennema, P. *J. Phys. D: Appl. Phys.* **1991**, *24*, 89.

55. Berkovitch-Yellin, Z. *J. Am. Chem. Soc.* **1985**, *107*, 8239.

56. Hartman, P.; Bennema, P. *J. Cryst. Growth* **1980**, *49*, 145.

57. Hartman, P.; Perdok, W. G. *Acta Crystallogr.* **1955**, *8*, 49-52.

58. Hartman, P.; Perdok, W. G. *Acta Crystallogr.* **1955**, *8*, 521-524.

59. Punzo, F. *Cryst. Growth Des.* **2011**, *11*, 3512-3521.

60. Hod, I.; Mastai, Y.; Medina, D. D. *CrystEngComm* **2011**, *13*, 502-509.

61. Zhang, C.; Ji, C.; Li, H.; Zhou, Y.; Xu, J.; Xu, R.; Li, J.; Luo, Y. *Cryst. Growth Des.* **2013**, *13*, 282-290.

62. Singh, M. K.; Banerjee, A. *Cryst. Growth Des.* **2013**, *13*, 2413-2425.

63. Zhukov, A.; Richards, O.; Ostanin, V.; Korchev, Y.; Klenerman, D. *Ultramicroscopy* **2012**, *121*, 1-7.

64. Happel, P.; Thatenhorst, D.; Dietzel, I. D. *Sens. Actuators, A* **2012**, *12*, 14983-15008.

65. Chen, C.-C.; Zhou, Y.; Baker, L. A. *ACS Nano* **2011**, *5*, 8404-8411.

66. Chen, C.-C.; Derylo, M. A.; Baker, L. A. *Anal. Chem.* **2009**, *81*, 4742-4751.

67. Momotenko, D.; McKelvey, K.; Kang, M.; Meloni, G. N.; Unwin, P. R. *Anal. Chem.* **2016**, *88*, 2838-2846.

68. Burt, H. M.; Mitchell, A. G. *Int. J. Pharm.* **1981**, *9*, 137-152.

69. Chernov, A. A. *Contemp. Phys.* **1989**, *30*, 251-276.

70. Perry, A. R.; Lazenby, R. A.; Adobes-Vidal, M.; Peruffo, M.; McKelvey, K.; Snowden, M. E.; Unwin, P. R. *CrystEngComm* **2015**, *17*, 7835-7843.

71. Ward, M. D. *Chem. Rev.* **2001**, *101*, 1697-1726.

72. Buller, R.; Peterson, M. L.; Almarsson, Ö.; Leiserowitz, L. *Cryst. Growth Des.* **2002**, *2*, 553-562.

73. Ran, Y.; He, Y.; Yang, G.; Johnson, J. L. H.; Yalkowsky, S. H. *Chemosphere* **2002**, *48*, 487-509.

74. Sangwal, K. *Etching of Crystals: Theory, experiment and application*; Elsevier, 2012.

For Table of Content Use Only

Face-discriminating dissolution kinetics of furosemide single crystals: In situ three-dimensional multimicroscopy and modeling

*Maria Adobes-Vidal, Faduma M. Maddar, Dmitry Momotenko, Leslie P. Hughes, Stephen A.C. Wren, Laura N. Poloni, Michael D. Ward and Patrick R. Unwin**

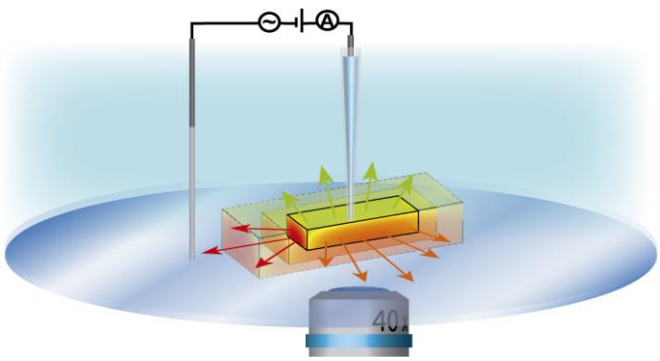

We present a versatile in situ multimicroscopy approach to study the dissolution kinetics of single crystals. The combination of optical microscopy and scanning ion-conductance microscopy measurements with finite element method (FEM) modeling allows the measurement of the dissolution rate of all the exposed crystal faces simultaneously, determination and quantification of the limiting process regulating dissolution.

Supporting Information

Face-discriminating dissolution kinetics of furosemide single crystals: In situ three-dimensional multimicroscopy and modeling

Maria Adobes-Vidal,[†] Faduma M. Maddar,[†] Dmitry Momotenko,[†] Leslie P. Hughes,[‡] Stephen A.C. Wren,[‡] Laura N. Poloni,[#] Michael D. Ward [#] and Patrick R. Unwin[*,†]*

†Electrochemistry and Interfaces Group, Department of Chemistry, University of Warwick, Coventry, CV4 7AL, United Kingdom, ‡Pharmaceutical Development, AstraZeneca, Macclesfield, SK10 2NA, United Kingdom, #Molecular Design Institute and Department of Chemistry, New York University, 100 Washington Square East, Silver Center, room 1001, New York, NY 1003, United States

Contents

Table S1. Crystallographic parameters of furosemide Polymorph I

Figure S1. Calculated and experimental PXRD patterns of furosemide form I

Table S2. Comparison of the optimized furosemide unit cell parameters and single crystal CCD X-ray diffraction data

Figure S2. UV–Vis spectra of furosemide dissolved in water at different concentrations

Table S3. Diffusive fluxes per unit area for each crystal face calculated from finite element simulation

Table S1. Crystallographic parameters for furosemide Polymorph I compared with literature.

	This study	**Babu *et al.****
Empirical formula	$C_{12}H_{11}ClN_2O_5S$	$C_{12}H_{11}ClN_2O_5S$
Formula weight	330.74	330.74
Temperature/K	150(2)	100(2)
Crystal system	triclinic	triclinic
Space group	P-1	P-1
a/Å	9.5355(5)	9.5150(9)
b/Å	10.4627(5)	10.4476(10)
c/Å	15.6209(7)	15.5826(16)
α/°	92.936(4)	92.839(2)
β/°	107.105(5)	107.088(2)
γ/°	116.498(5)	116.7470(10)
Volume/Å^3	1302.36(10)	1291.9(2)
Z	4	4
ρ_{calc} g/cm^3	1.648	1.700
m/mm^{-1}	0.425	0.482
Reflections collected	9208	13411
Independent reflections	5166	5061
Goodness-of-fit on F^2	1.045	1.050
Final R indexes [I>=2σ (I)]	R_1 = 0.0502	R_1 = 0.0668
Final R indexes [all data]	wR_2 = 0.1069	wR_2 = 0.1258

***** Babu, N. J.; Cherukuvada, S.; Thakuria, R.; Nangia, A. *Cryst. Growth Des.* **2010,** *10*, 1979-1989.

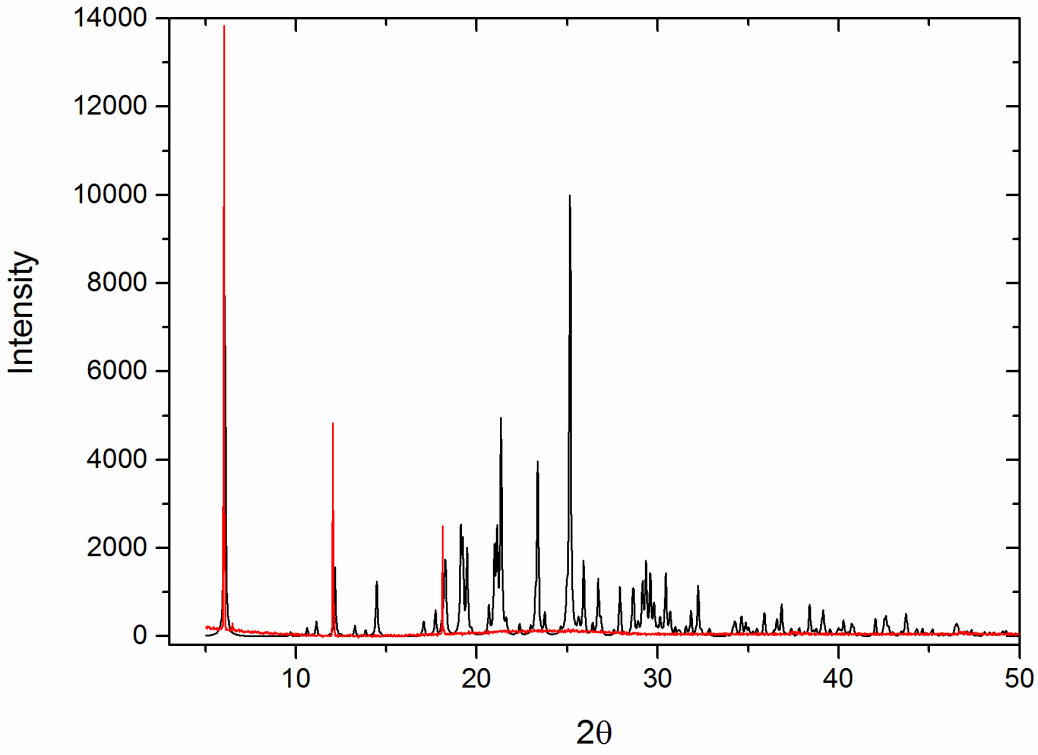

Figure S1. Calculated powder X-ray diffraction pattern of furosemide form I (black) and experimental (red) obtained for furosemide crystals mounted on a glass slide (λ = Cu-Kα, 0.1541 nm). The experimentally observed peaks at 2θ = 6.04°, 12.15° and 18.17° correspond to the (001), (002) and (003) reflections of polymorph I respectively, confirming the orientation of the raft-like crystals parallel to the glass slide.

Table S2. Comparison of the optimized furosemide unit cell parameters calculated using the COMPASS, Dreiding and cvff force fields and the experimental data obtained by single crystal CCD X-ray diffraction.

	Energy	**Unit cell parameters**					
	(kcal mol^{-1})	**a (Å)**	**b (Å)**	**c (Å)**	**A (º)**	**β (º)**	**γ (º)**
Experimental		9.5355	10.4627	15.6209	92.9360	107.1050	116.4980
COMPASS	-508.1135	9.8589	10.1926	14.7867	94.4689	106.0592	114.7914
Dreiding	-222.3405	9.7441	10.6284	15.6670	96.8028	108.2709	114.6225
cvff	-8.6023	10.3754	10.9100	15.8328	85.1591	110.7729	127.0457

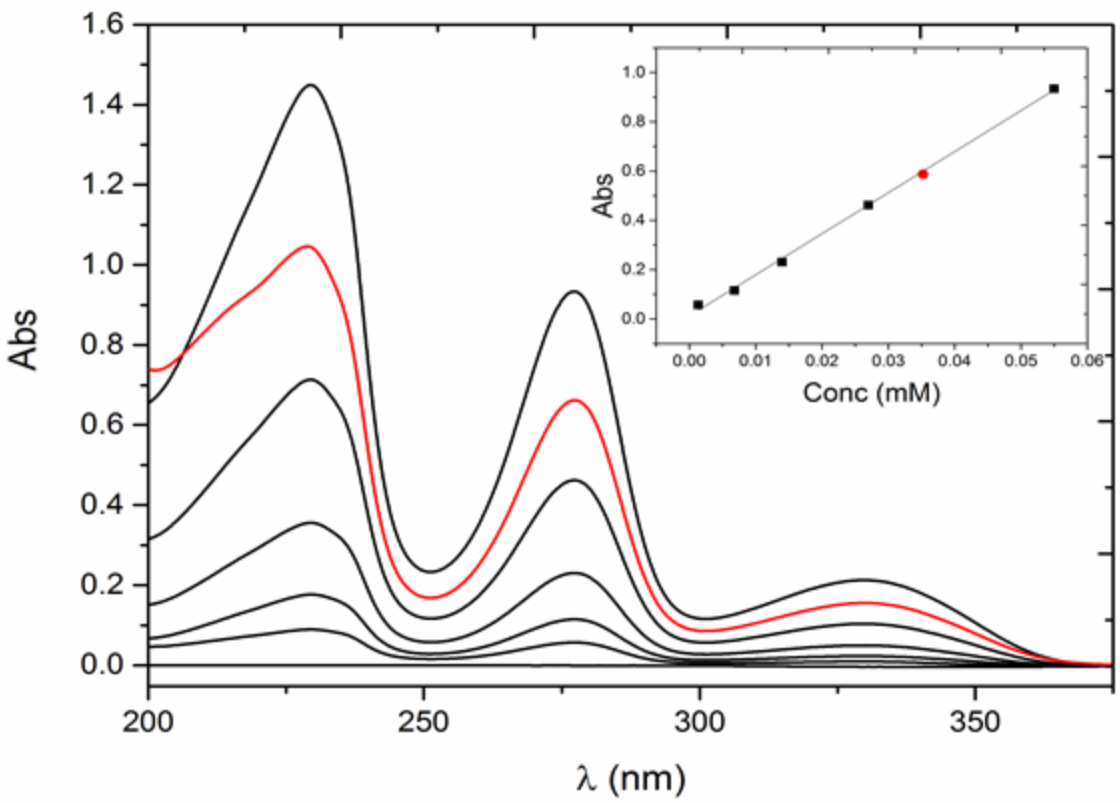

Figure S2. UV–Vis spectra of furosemide dissolved in water at different concentrations. Black lines show the UV–Vis spectra of furosemide in water at 0 mM, 0.0034 mM, 0.0068 mM, 0.014 mM, 0.027 mM and 0.055 mM used for calibration. The red line shows the UV–Vis spectra of a saturated solution of furosemide in water diluted 5 times. The inset shows the linear relationship between the absorbance and the concentration of furosemide at 277 nm. Black squares correspond to the calibration data and the red circle to the 5 times diluted saturated solution of furosemide in water.

Table S3. Diffusive fluxes per unit area for each crystal face calculated from finite element simulation of each studied crystal.

Face (hkl)	J_{Obs} (mol $m^{-2}s^{-1}$)	J_{MT} (mol $m^{-2}s^{-1}$)	J_{SK} (mol $m^{-2}s^{-1}$)
$(10\bar{1})$	5.2×10^{-6}	6.3×10^{-6}	Close to diffusion control
(010)	1.5×10^{-6}	5.1×10^{-6}	2.1×10^{-6}
(001)	0.6×10^{-6}	4.1×10^{-6}	0.7×10^{-6}
$(10\bar{1})$	9.2×10^{-6}	8.9×10^{-6}	Close to diffusion control
(010)	7.7×10^{-6}	7.3×10^{-6}	Close to diffusion control
(001)	4.4×10^{-6}	5.7×10^{-6}	Close to diffusion control
$(10\bar{1})$	13.6×10^{-6}	15.9×10^{-6}	Close to diffusion control
(010)	8.9×10^{-6}	12.3×10^{-6}	32.2×10^{-6}
(001)	0.9×10^{-6}	7.3×10^{-6}	1.0×10^{-6}
$(10\bar{1})$	14.5×10^{-6}	12.7×10^{-6}	Close to diffusion control
(010)	9.7×10^{-6}	10.6×10^{-6}	Close to diffusion control
(001)	2.1×10^{-6}	8.3×10^{-6}	2.8×10^{-6}
$(10\bar{1})$	20.3×10^{-6}	15.2×10^{-6}	Close to diffusion control
(010)	6.5×10^{-6}	10.8×10^{-6}	16.3×10^{-6}
(001)	3.6×10^{-6}	7.7×10^{-6}	6.7×10^{-6}

$(10\bar{1})$	15.3×10^{-6}	17.3×10^{-6}	Close to diffusion control [6]
(010)	22.2×10^{-6}	14.3×10^{-6}	Close to diffusion control
(001)	3.7×10^{-6}	8.4×10^{-6}	6.6×10^{-6}
$(10\bar{1})$	18.8×10^{-6}	16.4×10^{-6}	Close to diffusion control
(010)	16.6×10^{-6}	12.0×10^{-6}	Close to diffusion control
(001)	2.4×10^{-6}	6.7×10^{-6}	3.7×10^{-6}
$(10\bar{1})$	17.4×10^{-6}	19.2×10^{-6}	Close to diffusion control
(010)	17.9×10^{-6}	15.5×10^{-6}	Close to diffusion control
(001)	2.8×10^{-6}	6.8×10^{-6}	4.8×10^{-6}
$(10\bar{1})$	30.2×10^{-6}	23.3×10^{-6}	Close to diffusion control
(010)	22.4×10^{-6}	17.0×10^{-6}	Close to diffusion control
(001)	4.9×10^{-6}	11.0×10^{-6}	8.8×10^{-6}